Materials Transactions, Vol. 61, No. 7 (2020) pp. 1369 to 1380
©2020 Japan Foundry Engineering Society

Alloy Design and Fabrication of Ingots of Al–Mg–Li–Ca Light-Weight Medium Entropy Alloys*

Takeshi Nagase[1,2], Akira Terayama[3], Takashi Nagaoka[4], Nobuyuki Fuyama[4] and Tatsuaki Sakamoto[5]

[1]*Research Center for Ultra-High Voltage Electron Microscopy, Osaka University, Ibaraki 567-0047, Japan*
[2]*Division of Materials and Manufacturing Science, Graduate School of Engineering, Osaka University, Suita 565-0871, Japan*
[3]*Hiroshima Prefectural Technology Research Institute, Hiroshima 730-0031, Japan*
[4]*Western Region Industrial Research Center, Hiroshima Prefectural Technology Research Institute, Kure 737-0004, Japan*
[5]*Department of Materials Science and Biotechnology, Graduate School of Science and Engineering, Ehime University, Matsuyama 790-8577, Japan*

Alloy designs of light-weight high and medium entropy alloys (LW-HEA and LW-MEA, respectively) are discussed in relation to solving the problem of the empirical alloy parameter, ΔH_{mix}, and the difficulties of the fabrication process. The ingots of newly-designed Al–Mg–Li–Ca LW-MEAs were fabricated by the conventional casting process via crucible melting without using a vacuum furnace, and casting under air atmosphere. The ΔH_{mix} parameter is the average value of the mixing enthalpy of $\Delta H_{\mathrm{i\text{-}j}}$ between the two components, i-j, in the multicomponent alloys, and the dispersion of $\Delta H_{\mathrm{i\text{-}j}}$ cannot be evaluated. The parameter $\delta(\Delta H_{\mathrm{mix}})$ was suggested for the evaluation of the dispersion of $\Delta H_{\mathrm{i\text{-}j}}$. The Al–Mg–Li–Ca LW-MEAs were designed based on the empirical alloy parameters, including $\delta(\Delta H_{\mathrm{mix}})$. The alloy ingots of equiatomic AlMgLiCa, non-equiatomic $Al_2MgLiCa$, and $AlMgLiCa_{0.3}$ were successfully obtained by the conventional casting process. The solidification microstructure of the ingots in the $Al_2MgLiCa$ LW-MEA was investigated, with particular focus on the position dependences of the chemical composition, constituent phases, solidification microstructure, and hardness. The present study clarified that LW-HEAs and LW-MEAs containing Al, Mg, Li, and Ca can be obtained by the conventional casting process under air atmosphere, without specific expensive casting equipment. [doi:10.2320/matertrans.F-M2020825]

(Received January 30, 2020; Accepted April 3, 2020; Published June 5, 2020)

Keywords: *high entropy alloy (HEA), medium entropy alloy (MEA), aluminum alloy, magnesium alloy, lithium alloy, calcium alloy, melting, metallic mold casting*

1. Introduction

A new class of structural and functional materials, called as high-entropy alloy (HEA), has been suggested.[1–7] The research interest with HEAs has been growing. In general, HEAs were previously classified as alloys possessing the following properties: (1) the number of constituent elements were five or more, (2) their atomic compositions were equal to the equiatomic composition ratio or close to it, (3) they had a single solid solution phase. Thus far, various concepts and definitions of HEAs have been proposed and changed gradually. The general criterion among the researchers is not existed currently. Not only alloys with single solid solution phases but also those with multi-solid solution phases and intermetallic compounds are also called as HEAs. Among the various definitions of HEAs, the following is based on the mixing entropy (ΔS_{mix}) and is widely recognized.[5,6]

$$\Delta S_{mix} = -R \cdot \sum_{i=1}^{n} x_i \cdot \ln(x_i), \tag{1}$$

$$\Delta S_{mix} \geq 1.5R \text{ (HEA)}, \tag{2}$$

where ΔS_{mix} is the mixing entropy of ideal solutions and regular solutions, R is the gas constant (8.314 J/K mol), x_{i} is the mole fraction of the i-th element. Based on the above entropy-based alloy definition, the definitions of medium-entropy alloys (MEAs) and low-entropy alloys (LEAs) have also been proposed.

$$1.0R \leq \Delta S_{mix} \leq 1.5R \text{ (MEA)} \tag{3}$$

$$\Delta S_{mix} \leq 1.0R \text{ (LEA)} \tag{4}$$

In the present study, the alloys were classified as per the entropy-based definitions as denoted in eqs. (1)–(4). The classification of conventional casting metals, including cast irons, is available in the literature.[8,9] There are almost no existing conventional casting alloys that are HEAs satisfying eq. (2). A few high-alloy cast irons are classified as MEAs among conventional casting metals.

HEAs were suggested to show four core effects which was not observed in common and/or single-element-based alloys.[5,6] The four core effects are summarized as follows: (1) high entropy effect, (2) severe lattice distortion effect, (3) sluggish diffusion effect, and (4) cocktail effect. Considering that HEAs are cast materials, they exhibit the following interesting effects:[8–11] (1) the solid solution phase was obtained due to the high entropy effect using the conventional casting without requiring unique techniques and equipment, (2) ductile materials can be obtained owing to the formation of a solid solution, and (3) high-strength materials are formed because of the severe lattice distortion in the ingots. Thus, HEAs were of interest as the casting alloys.

In recent years, Youssef and Koch *et al.* reported the development of light-weight HEA (LW-HEA) as a new family of HEAs at 2015. They fabricated the bulk specimens

*This Paper was Originally Published in Japanese in J. JFS **91** (2019) 717–729. Minor corrections in abstract, main text, figure and table captions, and references were performed with translation from Japanese to English and proof reading by native speakers. Some references written in Japanese was replaced by the related references written in English: Ref. 11) was changed from "the 24th Committee on casting of Japan Society for the Promotion of Science (JSPS), Subcommittee on casting process, the 20th meeting document, No. 22 (2018) 1–5." to "Mater. Des. **184** (2019) 108172". Ref. 41) was changed from "J. Soc. Mater. Sci., Japan **68** (2019) 205–211." to "Mater. Trans. **61** (2020) 311–317".

of the $Al_{20}Li_{20}Mg_{10}Sc_{20}Ti_{30}$ LW-HEA with HCP or FCC solid solutions by mechanical milling and the powdered metallurgy process.[12] The fabrication of the bulk specimens and/or ingots of LW-HEAs by arc-melting process was reported in $Al_xCrFeMnTi_y$ LW-HEAs[13,14] and AlCrTiV LW-MEAs[15] as the challenge for the application of casting process in LW-HEAs. These LW-HEAs and LW-MEAs contain Cr and Fe, which increase their densities, whereas the contained Ti makes their fabrication via the conventional casting process with crucible melting and casting in air atmosphere difficult. The fabrication of the ingots of AlMgLiCaCu LW-HEAs via the casting process is reported as the challenge for the fabrication of bulk specimens in LW-HEAs. A single solid solution phase formation was realized by Li *et al.*; however, a detailed analysis of the X-ray diffraction (XRD) patterns demonstrated that this did not occur in the ingots.[16] Furthermore, the detailed information for the casting process was not denoted. Regarding the fabrication of the ingots of LW-HEAs via the casting process via crucible melting and high frequently melting under inert gas, experiments were conducted for $Mg_xMnAlZnSn$,[17] $Mg_xAlZnCuSn$,[18] $MgAl_xZnCuSn$,[18] and $MgAlZnCuSn_x$[18] LW-HEAs; however, the formation of single solid solution phases was not achieved. In a review paper published in 2018 about LW-HEAs,[19] little was reported about LW-HEAs with a single solid solution phase. Despite the demand of LW-HEAs as the new light-weight structural metallic materials because of its low density, high mechanical strength and ductility, their development has not progressed steadily. The major difficulties in synthesizing HEAs containing low-density elements are as follows:[19] (1) the difficulty in alloy design, and (2) the difficulty in the fabrication processes. Elements Al, Ti, Mg, Li, Ca, and Be are considered suitable because of their low density and the common metallic materials for practical usage. From the perspective of the fabrication of the bulk specimens of LW-HEAs by the casting process, Ti and Mg elements are not favorable because of the high reactivity between the molten metals and the crucibles and that between the molten metals and the environment related to the ignition tendency. The difficulty in the application of the casting process in Ti alloys has been previously discussed in detail based on their comparison with plastic working and powder metallurgy,[20,21] the precision casting process,[22] and dental science and engineering and dental precision casting.[23,24] Ti has excellent corrosion resistance in the solid state; however, its molten state is significantly active under atmospheric gases and crucibles. In addition, most of the reaction products dissolve in the molten metal and can barely be removed, thereby degrading the quality of the casting products. Above-described problems leads to the situation that the proportion of castings in the production of formed and fabricated materials in Ti and Ti alloys is extremely low. The preparation of the ingots of alloys containing Li and/or Ca elements by the casting process is difficult because of their high reactivity in their solid states at room temperature as well as in the molten states at and above the melting temperature. For alloys with a high content of Be, the application of the casting process for the fabrication of their ingots is difficult, because of the Be fume toxicity. For the mass production of the bulk specimens of HEAs and MEAs, the casting process is basically superior to other production processes because the mixing of the multi-component elements can be easily achieved in the molten state. Simultaneously, the following three points must be considered for the employment of the casting process to HEAs and MEAs:[8–11] (1) The casting process is not established for alloys with differences in the melting temperature, reactivity with crucibles, a degree of oxidation, and vapor pressure among constituent elements. (2) There is a possibility for the segregation during solidification and the inhomogeneous in chemical composition. (3) Coarse crystal grains are easier to form in the ingots by the casting process than in the bulk specimens obtained by powder metallurgy. There are numerous unsolved issues in the application of the casting method to HEAs and MEAs, even in the problems (1). For LW-HEAs and LW-MEAs, the application of powder metallurgy and/or the arc melting process is the mainstream,[19] and a systematic research on the employment of conventional casting processes to multi-component alloys, including LW-HEAs and LW-MEAs, is yet to be performed. In this paper, the following two topics about LW-HEAs and LW-MEAs are reported for the development of new LW-HEAs and LW-MEAs as casting alloys. (1) Conducting the alloy design for LW-HEAs and LW-MEAs, and (2) The discussion whether the application of the casting processes is feasible for the fabrication of the ingots in multi-component alloys containing light-weight metallic elements. The paper reported that the ingot can be produced by the conventional casting process via crucible melting under the inert gas flow and the pouring in air atmosphere in multicomponent alloy, even for multicomponent light-weight alloys composed of light-weight elements.

2. Alloy Design

Empirical alloy parameters are widely used for the prediction of the solid solution formation tendency of multi-component alloys, including HEAs and MEAs.[5,6] Among them, the following five parameters are recognized as the typical alloy parameters and are effective in designing HEAs and MEAs as casting alloys:

(A) Mixing entropy, ΔS_{mix}
(B) Mixing enthalpy, ΔH_{mix}
(C) Delta parameter, δ
(D) Omega parameter, Ω
(E) Valence electron concentration parameter, *VEC*

The review for the application of above-described parameters in HEAs for casting alloys was reported in the literature.[8] The mixing enthalpy (ΔH_{mix}) is expressed in eq. (5).

$$\Delta H_{\mathrm{mix}} = 4 \sum_{j \neq i} \sum_{i} x_{\mathrm{i}} x_{\mathrm{j}} \Delta H_{\mathrm{i\text{-}j}}, \tag{5}$$

where $\Delta H_{\mathrm{i\text{-}j}}$ is the mixing enthalpy of an A(i-th element)–B(j-th element) binary system at the equiatomic composition ($A_{50}B_{50}$) for the liquid phase. The values of $\Delta H_{\mathrm{i\text{-}j}}$ were obtained from the literature.[25] Zhang *et al.* reported that $-20 \leq \Delta H_{\mathrm{mix}} \leq 5$ [kJ/mol] to be favorable for solid solution formation in multi-component alloys.[3] Guo *et al.* suggested that the tendency of solid solution formation was enhanced when $-11.6 \leq \Delta H_{\mathrm{mix}} \leq 3.2$.[26] These indicate that the absolute value of $\Delta H_{\mathrm{mix}} = 0$ is favorable for solid solution

formation. ΔH_{mix} is a parameter for explaining the interaction between the constituent elements in multi-component alloys. The closer ΔH_{mix} is to zero, the smaller is the above-mentioned interaction, resulting in the suppression of the formation of intermetallic HEAs and MEAs.[5,6] The δ parameter is used for evaluating the differences in the atomic radii of the constituent elements in multi-component alloys. The lower the value of δ, the higher the tendency of solid solution formation in the multi-component alloy.[5,6] Yang *et al.* suggested a dimensionless Ω parameter, and the condition of $\Omega \geq 1.1$ was found to be favorable for the formation of a solid solution in multi-component alloys.[27] The Ω parameter includes ΔH_{mix} in the denominator and ΔS_{mix} in the numerator. Therefore, when ΔH_{mix} is small and ΔS_{mix} is large, the Ω parameter is large. It is pointed out in HEAs, not only achieving solid solution stabilization by simply increasing ΔS_{mix} but also the relative size relationship between ΔH_{mix} and ΔS_{mix} needs to be considered.[7] The Ω parameter is widely used for discussing the relative relationship between ΔH_{mix} and ΔS_{mix}.

Figure 1 shows the $\Delta H_{i\text{-}j}$ matrix of a typical HEA system, in which: (a) Co–Cr–Fe–Mn–Ni is a typical example of a 3d transition-metal-type HEA (3d-HEA),[1] (b) Ti–Nb–Ta–Zr–Hf is a typical example of a refractory HEA (RHEA),[28–30] and (c) Al–Ti–Li–Mg–Sc is a typical example of an LW-HEA.[12] In Fig. 1, the blue and red letters denote the cases of $\Delta H_{mix} \leq -10$ kJ/mol and $\Delta H_{mix} \geq 10$ kJ/mol, respectively, where 10 kJ/mol was used as the standard for the value of ΔH_{mix}. The Co–Cr–Fe–Mn–Ni (Fig. 1(a)) and Ti–Nb–Ta–Zr–Hf (Fig. 1(b)) systems present the low $\Delta H_{i\text{-}j}$ values (the absolute values of $\Delta H_{i\text{-}j}$ are below 10 for the constituent elements), resulting in a low absolute value of ΔH_{mix}. In contrast, the Al–Ti–Li–Mg–Sc system (Fig. 1(c)) exhibits a tendency for various large positive $\Delta H_{i\text{-}j}$ and large negative $\Delta H_{i\text{-}j}$, despite the low absolute value of ΔH_{mix}. The equiatomic CoCrFeMnNi 3d-HEA, the equiatomic TiNbTaZrHf RHEA, and $Al_{20}Li_{20}Mg_{10}Sc_{20}Ti_{30}$ LW-HEA presents low absolute values of ΔH_{mix}, however, the properties of the series of the $\Delta H_{i\text{-}j}$ values of the $Al_{20}Li_{20}Mg_{10}Sc_{20}Ti_{30}$ LW-HEA are different from those of the $\Delta H_{i\text{-}j}$ values of the equiatomic CoCrFeMnNi and TiNbTaZrHf HEAs, resulting in the lower solid solution formation tendency and the harder for the application of casting process in $Al_{20}Li_{20}Mg_{10}Sc_{20}Ti_{30}$ LW-HEA than equiatomic CoCrFeMnNi 3d-HEA, the equiatomic TiNbTaZrHf RHEA.

It is well known that the solidification behavior and the constituent phases formed by the solidification of alloys are affected by the $\Delta H_{i\text{-}j}$ of their constituent elements. Amorphous phase formation was reported to be found in alloys with large negative $\Delta H_{i\text{-}j}$ of their constituent elements, owing to the stabilization of their liquid phase.[31] In contrast, liquid phase separation was found in immiscible alloys with large positive $\Delta H_{i\text{-}j}$ values of their constituent elements, owing to the destabilization of their liquid phase and the enhancement of the immiscibility.[32] A multi-component alloy with both large negative and positive $\Delta H_{i\text{-}j}$ values of its constituent elements is a particular alloy with a tendency of both the stabilization and destabilization of its liquid phase. Immiscible alloys with liquid phase separation and amorphous phase formation, which are called "liquid-phase-separation-type amorphous alloys," are known as the typical examples of multi-component alloys with large negative and positive $\Delta H_{i\text{-}j}$ values of its constituent elements.[33–35] Based on the alloy design technique for multi-component alloys with large negative and positive $\Delta H_{i\text{-}j}$ of its constituent elements,[36] various liquid-phase-separation-type amorphous alloys, including Fe–Cu,[37,38] Fe–Ag,[39] Cu–Ag–Fe,[40,41] Co–Cu,[42,43] and Al–Pb-based alloys,[44] have been developed. In the material processing for the fabrication of liquid-phase-separation-type amorphous alloys, melting and casting are difficult, because of the high vapor pressures of the particular constituent elements that have large positive $\Delta H_{i\text{-}j}$. There is difficulty in the alloy design and the fabrication of liquid-phase-separation-type amorphous alloys. This indicates that there is a significant dissimilarity in the same for HEAs with various $\Delta H_{i\text{-}j}$ values of ~0 (such as the equiatomic CoCrFeMnNi 3d-HEA and the equiatomic TiNbTaZrHf RHEA) and HEAs with large negative and positive $\Delta H_{i\text{-}j}$ values (such as $Al_{20}Li_{20}Mg_{10}Sc_{20}Ti_{30}$ LW-HEA). This is despite the low absolute values of their ΔH_{mix}. Specifically, alloys with numerous large positive and negative $\Delta H_{i\text{-}j}$ are considered to have a lower solid solution forming ability and have difficulty in melting and casting compared to alloys with various $\Delta H_{i\text{-}j}$ close to zero.

The parameter of ΔH_{mix} of multi-component alloys corresponds to the compositional average of the $\Delta H_{i\text{-}j}$ values. Figure 2 shows the $\Delta H_{i\text{-}j}$ matrices of quaternary A–B–C–D model alloy systems for discussing the difference in ΔH_{mix} and $\delta(\Delta H_{mix})$, where $\delta(\Delta H_{mix})$ is the parameter for evaluating the dispersion of the $\Delta H_{i\text{-}j}$ of the constituent elements in multi-component alloys and can be obtained by eq. (6).

$$\delta(\Delta H_{mix}) = 4\sum_{j\neq i}\sum_{i} x_i x_j |\Delta H_{i\text{-}j} - \Delta H_{mix}|, \quad (6)$$

where $|\Delta H_{i\text{-}j} - \Delta H_{mix}|$ is the absolute value of $(\Delta H_{i\text{-}j} - \Delta H_{mix})$. Figure 2(a) presents model alloy X as a typical alloy

(a) Co-Cr-Fe-Mn-Ni

	Co	Cr	Fe	Mn	Ni
Co		-4	-1	-5	0
Cr			-1	2	-7
Fe				0	-2
Mn					-8
Ni					

(b) Ti-Nb-Ta-Zr-Hf

	Ti	Nb	Ta	Zr	Hf
Ti		2	1	0	0
Nb			0	4	4
Ta				3	3
Zr					0
Hf					

(c) Al-Ti-Li-Mg-Sc

	Al	Ti	Li	Mg	Sc
Al		-30	-4	-2	-38
Ti			34	16	8
Li				0	12
Mg					-3
Sc					

Fig. 1 $\Delta H_{i\text{-}j}$ matrix of typical HEA system. (a) Co–Cr–Fe–Mn–Ni as 3d-HEA, (b) Ti–Nb–Ta–Zr–Hf as RHEA, (c) Al–Ti–Li–Mg–Sc as LW-HEA.

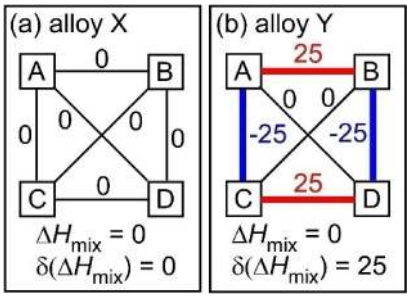

Fig. 2 $\Delta H_{i\text{-}j}$ matrix of quaternary A–B–C–D model alloy systems. (a) alloy systems with significant weak interaction among the constituent elements. (b) alloy systems with strong repulsive ($\Delta H_{i\text{-}j} \gg 0$, positive) and interactive ($\Delta H_{i\text{-}j} \ll 0$, negative) interactions among the constituent elements.

system with an extremely weak interaction between its constituent elements, so that all combination of $\Delta H_{i\text{-}j}$ are 0. In model alloy X, the values of both ΔH_{mix} and $\delta(\Delta H_{mix})$ are 0. Liquid phase separation and amorphous phase formation based on $\Delta H_{i\text{-}j}$ barely occur, resulting in a high solid solution formation tendency. Figure 2(b) shows model alloy Y as the typical alloy system with strong repulsive ($\Delta H_{i\text{-}j} \gg 0$, positive) and interactive ($\Delta H_{i\text{-}j} \ll 0$, negative) interactions between the constituent elements. Model alloy Y has the following two possibilities: (1) The feature of $\Delta H_{mix} = 0$ increases the possibility of forming a single-phase solid solution when the constituent elements can be mixed thoroughly in both the liquid and solid states. (2) Under the influence of the dispersion of $\Delta H_{i\text{-}j}$ (large positive values of $\Delta H_{i\text{-}j}$), the A–C and B–D liquid phases are separated during the solidification process. In comparison, the large negative values of $\Delta H_{i\text{-}j}$ generate liquid-separated amorphous alloys, such as the A–C and B–D amorphous phases. Alternatively, they lead to a multiphase structure consisting of A–C and B–D intermetallic compounds. The production of numerous liquid-phase-separation-type amorphous alloys and the solid solution formation in multi-component alloys through the solidification route via casting process indicate that besides a low absolute value of ΔH_{mix}, the strategy of realizing a low absolute value of $\delta(\Delta H_{mix})$ is important for the development of HEAs.

Table 1 lists the alloy parameters of $\Delta S_{mix}/R$, ΔH_{mix}, and $\delta(\Delta H_{mix})$ and provides the reported structures of various alloys, including typical 3d-HEAs (Group A), RHEAs (Group B), amorphous alloys (Group C), liquid-phase-separation-type amorphous alloys (Group D), LW-HEAs and LE-MEAs (Group E), and Al–Li–Mg and Al–Li–Mg–Ca alloys (Group F). The notations of S.S, Am., and Am.(dual) indicate solid solution, a single amorphous phase, and dual amorphous phases related with liquid-phase-separation-type amorphous alloys, respectively. Figure 3 shows the $\delta(\Delta H_{mix})$-ΔH_{mix} maps for the various alloys listed in Table 1. In Fig. 3, the values of $\delta(\Delta H_{mix})$ and ΔH_{mix} of the 3d-HEAs (Group A) and RHEAs (Group B) are close to 0. LW-HEAs and LE-MEAs (Group E) exhibit a tendency of ΔH_{mix} close to 0 and large positive values of $\delta(\Delta H_{mix})$ around 20 kJ/mol. In the $\delta(\Delta H_{mix})$-ΔH_{mix} map, the LW-HEAs and LE-MEAs (Group E) are positioned in a different zone from those of the 3d-HEAs (Group A) and RHEAs (Group B). The amorphous alloys (Group C) present a large negative ΔH_{mix} and a wide range of values of $\delta(\Delta H_{mix})$. Based on the alloy design of amorphous alloys,[25,31] a large negative ΔH_{mix} is recognized to be important for increasing the glass forming ability (GFA), whereas there is no restriction on the dispersion of $\Delta H_{i\text{-}j}$. The liquid-phase-separation-type amorphous alloys (Group D) have a tendency for positive and negative $\Delta H_{i\text{-}j}$, resulting in smaller absolute values of ΔH_{mix} and larger absolute values of $\delta(\Delta H_{mix})$ (around 20 kJ/mol) than those of amorphous alloys (Group C). It should be noted here that in the $\delta(\Delta H_{mix})$-ΔH_{mix} map, the region of the LW-HEAs (Group E) overlaps with that of the liquid-phase-separation-type amorphous alloys (Group D). These characteristics of the $\delta(\Delta H_{mix})$-ΔH_{mix} map indicate the $\delta(\Delta H_{mix})$ parameter is effective for evaluating the deviation in the $\Delta H_{i\text{-}j}$ of multi-component alloys, including 3d-HEAs (Group A), RHEAs (Group B), and LW-HEAs and LW-MEAs (Group E). The decrease in the absolute values of $\delta(\Delta H_{mix})$ is considered to be important for the formation of a solid solution phase in multi-component alloys.

Table 1 Alloy parameters of $\Delta S_{mix}/R$, ΔH_{mix} and $\delta(\Delta H_{mix})$ and the reported structure in various alloys including typical 3d-HEA (Group A), RHEA (Group B), amorphous alloy (Group C), liquid-phase-separation type amorphous alloy (Group D), LW-HEA (Group E), Al–Li–Mg and Al–Li–Mg–Ca alloys (Group F). The notation of S.S, Am., Am.(dual) means solid solution, an amorphous phase, and dual amorphous phases, respectively.

	Alloys	$\Delta S_{mix}/R$	ΔH_{mix}	$\delta(\Delta H_{mix})$	Structure
A	CoCrFeMnNi	1.61	-4.2	4.9	S.S.
	$CoCrFe_2MnNi$	1.56	-3.3	4.2	S.S.
	$CoCrFe_3MnNi$	1.48	-2.8	3.4	S.S.
	CoCuFeMnNi	1.61	0.3	7.2	S.S.
	$CoCu_2Fe_2MnNi$	1.55	3.5	9.1	S.S.
	CoCrFeMnNiCu	1.79	2.2	8.1	S.S.
	$CoCrFeMnNiCu_2$	1.75	4.8	8.3	S.S.
	$CoCrFeMnNiCu_3$	1.67	6.1	7.8	S.S.
	$Al_{0.3}CoCrCuFeNi$	1.74	-4.6	8.8	S.S.
B	NbMoTaW	1.39	-6.5	4.3	S.S.
	VNbMoTaW	1.61	-4.6	5.2	S.S.
	TiNbTaZr	1.39	2.5	2.3	S.S.
	TiNbTaZrHf	1.61	2.7	2.6	S.S.
	TiNbTaZrV	1.61	0.3	3.0	S.S.
	TiNbTaZrMo	1.61	-1.8	5.5	S.S.
	TiNbTaZrW	1.61	-3.0	7.2	S.S.
C	$Ni_{20}Nb_{20}Zr_{20}$	0.95	-37.3	15.7	Am.
	$Zr_{65}Al_{7.5}Cu_{27.5}$	0.83	-25.1	7.2	Am.
	$Zr_{60}Al_{20}Ni_{20}$	0.95	-48.2	6.6	Am.
	$Zr_{65}Al_{7.5}Ni_{10}Cu_{17.5}$	1.39	-33.8	29.6	Am.
	$Zr_{41.2}Ti_{13.8}Cu_{12.5}Ni_{10}Be_{22.5}$	1.46	-36.7	27.0	Am.
	$Ti_{34}Zr_{11}Cu_{47}Ni_8$	1.17	-40.8	22.3	Am.
	$Mg_{65}Cu_{15}Y_{10}Ag_{10}$	1.03	-7.7	5.2	Am.
	$Ca_{60}Mg_{20}Ag_{10}Cu_{10}$	1.09	-13.0	9.3	Am.
	$La_{27.5}Zr_{27.5}Al_{25}Cu_{10}Ni_{10}$	1.52	-34.0	29.1	Am.(dual)
	$Y_{28}Ti_{28}Al_{24}Co_{20}$	1.38	-28.4	20.0	Am.(dual)
	$Ni_{58.5}Nb_{20.25}Y_{21.25}$	1.10	-15.1	32.9	Am.(dual)
D	$Fe_{50}Cu_{20}Zr_{10}B_{20}$	1.22	-17.7	24.6	Am.+S.S.
	$Fe_{60}Cu_{12}Nb_8B_{20}$	1.08	-15.2	18.1	Am.+S.S.
	$Fe_{52.5}Cu_{30}Si_7B_{10.5}$	1.12	-4.7	22.4	Am.+S.S.
	$Fe_{52.5}Ag_{30}Si_7B_{10.5}$	1.12	5.3	29.9	Am.+S.S.
	$Co_{52.5}Cu_{30}Si_7B_{10.5}$	1.12	-9.1	19.2	Am.+S.S.
	$Al_{20}Ti_{30}Li_{20}Mg_{10}Sc_{20}$	1.56	-0.4	28.3	S.S.
E	$Al_{38}Cr_{19}Fe_{19}Mn_{19}Ti_5$	1.46	-14.9	12.1	S.S.
	AlCrTiV	1.39	-16.8	15.0	S.S.
F	AlLiMg	1.10	-2.7	2.1	
	AlLiMgCa	1.39	-8.3	10.0	
	$Al_2LiMgCa$	1.33	-9.4	10.9	
	$AlLiMgCa_{0.3}$	1.30	-5.2	5.7	

For the Al–Ti–Mg–Li–Sc alloys, the $\Delta H_{i\text{-}j}$ values of the Ti–Mg and Ti–Li atomic pairs are large positive values ($\Delta H_{i\text{-}j} \geqq 10$ kJ/mol), whereas those of Al–Ti and Al–Sc are large negative values, as shown in Fig. 1(c). This indicates that the Al–Mg–Li alloy system without Ti–Mg, Ti–Li, Al–Ti, and Al–Sc atomic pairs has low absolute values of ΔH_{mix} and $\delta(\Delta H_{mix})$. The values of $\Delta H_{i\text{-}j}$ of Al, Mg, and Li are near zero, resulting in significantly low values of ΔH_{mix} and

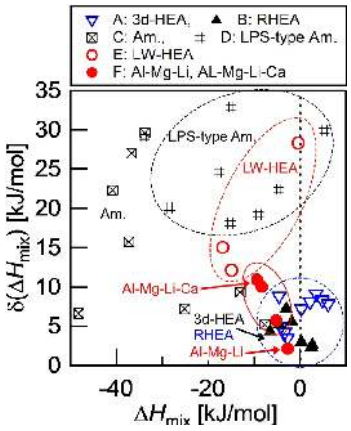

Fig. 3 $\delta(\Delta H_{mix})$-ΔH_{mix} maps in various alloys including typical 3d-HEA (Group A), RHEA (Group B), amorphous alloys (Group C), liquid-phase-separation type amorphous alloy (Group D), LW-HEAs (Group E), Al–Li–Mg and Al–Li–Mg–Ca alloys (Group F).

	Al	Mg	Li
Al		−2	−4
Mg			0
Li			

+

Ti	Ca	Cr	V
−30	−20	−10	−16
16	−6	24	23
34	−1	36	37

Fig. 4 Alloy design of Al–Mg–Li–X (X = Ti, Ca, Cr and V) alloy systems focusing on $\Delta H_{i\text{-}j}$ matrix.

$\delta(\Delta H_{mix})$ of the Al–Mg–Li alloy system. In fact, the absolute values of ΔH_{mix} and $\delta(\Delta H_{mix})$ of the equiatomic AlMgLi alloy are significantly small: $\Delta H_{mix} = -2.7\,kJ/mol$ and $\delta(\Delta H_{mix}) = 2.1\,kJ/mol$, as shown in Table 1. Combining Al, Mg, and Li is considered to be suitable for the formation of a solid solution phase in the ingots prepared by the casting process. As candidates for the X element in the Al–Mg–Li–X alloy system from ternary Al–Mg–Li alloy system, Ca, as a light-weight metallic element, and Cr and V, which are the constituent elements of $Al_xCrFeMnTi_y$[13,14] and AlCrTiV[15] LW-HEAs and LW-MEAs, were considered. Figure 4 shows the alloy design of Al–Mg–Li–X (X = Ti, Ca, Cr, and V) alloy systems by focusing on the $\Delta H_{i\text{-}j}$ matrix, where Al–Mg–Li–Ti alloy system is considered as the reference. The values of $\Delta H_{i\text{-}j}$ (i = Al, Mg, Li) (j = Ti, Cr, V) are either large positive or large negative values. With Ca, $\Delta H_{i\text{-}j}$ (i = Mg, Li) (j = Ca) has small absolute values, and only $\Delta H_{i\text{-}j}$ (i = Al) (j = Ca) has large negative values. These indicate that Ca is more suitable than Cr and V as the candidate X element in the Al–Mg–Li–X alloy system. Based on the entropy-based definition (eqs. (1) and (2)), quaternary Al–Mg–Li–Ca alloys cannot satisfy $\Delta S_{mix} \geq 1.5R$. However, a quaternary Al–Mg–Li–Ca alloy system was selected as the basic study to explore the possibility of producing LW-HEA and LW-MEA ingots by the casting method, particularly for the conventional crucible melting under inert gas atmosphere and mold-casting in air atmosphere. The ingots of equiatomic AlMgLiCa ($Al_{25}Mg_{25}Li_{25}Ca_{25}$, at%) alloy and non-equiatomic Al–Mg–Li–Ca alloy were fabricated by the casting process, where the possibility for the solid solution formation in Al–Mg–Li–Ca alloy were discussed based on the empirical alloy parameters of HEAs. As non-equiatomic Al–Mg–Li–Ca alloys, $Al_xMgLiCa$ alloys (x > 1), which are Al-rich alloys,

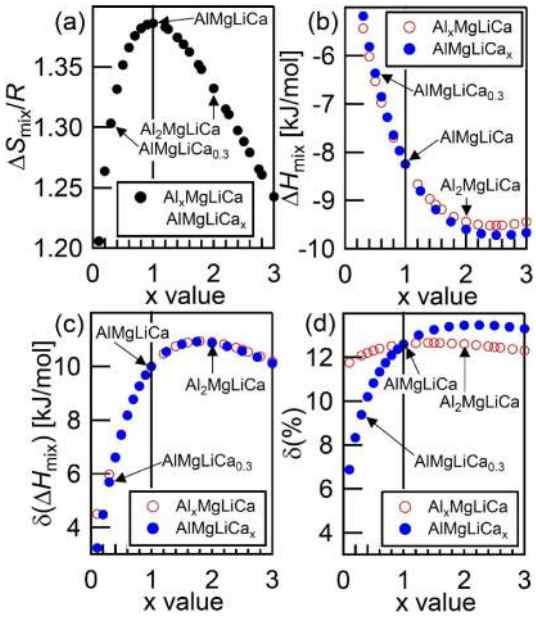

Fig. 5 Alloy design of $Al_xMgLiCa$ and $AlMgLiCa_x$ alloys using empirical alloy parameters. (a) $\Delta S_{mix}/R$, (b) ΔH_{mix}, (c) $\delta(\Delta H_{mix})$, (d) δ.

and $AlMgLiCa_y$ (y < 1) alloys were considered for the ease of casting.

Figure 5 exhibits the x value dependence on the empirical alloy parameters in the $Al_xMgLiCa$ and $AlMgLiCa_x$ alloys using empirical alloy parameters. In Fig. 5(a), the increase in x decreases $\Delta S_{mix}/R$. $\Delta S_{mix}/R$, reaching a value of 1.0 or more, which is corresponding to an MEA, over a wide range of $0.1 \leqq x \leqq 3$. Figure 5(b) presents the x value dependence on the ΔH_{mix} of the $Al_xMgLiCa$ and $AlMgLiCa_x$ alloys. The absolute value of ΔH_{mix} increases negatively with the increase in x, and ΔH_{mix} reaches approximately $-10\,kJ/mol$ at approximately $x \geqq 2$. In Fig. 5(c), the increase in x decreases $\delta(\Delta H_{mix})$ in the region where $x \leqq 1$, and the value of $\delta(\Delta H_{mix})$ becomes almost $10\,kJ/mol$ in the region where $x \geqq 1$. Figure 5(d) shows the differences in the x value dependence on δ of the $Al_xMgLiCa$ and $AlMgLiCa_x$ alloys. The increase in the x value leads to a significant increase in the value of δ of the $AlMgLiCa_x$ alloys, whereas the x dependence on the δ value of the $Al_xMgLiCa$ alloys is small. Based on the above-described empirical alloy parameters of the Al–Mg–Li–Ca alloys, the ingots of $Al_2MgLiCa$ ($Al_xMgLiCa$ (x = 2)) and $AlMgLiCa_{0.3}$ ($AlMgLiCa_x$ (x = 0.3)) alloys were fabricated by the casting process. Table 2 lists the alloy parameters of $\Delta S_{mix}/R$, ΔH_{mix}, $\delta(\Delta H_{mix})$, δ, and Ω for predicting the solid solution formation tendencies of the LW-HEAs (Group E), Ti-containing alloys (Group G), and Al–Mg–Li and Al–Mg–Li–Ca alloys not containing Ti (Group F). The $Al_{20}Li_{20}Mg_{10}Sc_{20}Ti_{30}$ LW-HEA[12] in Group E has a high solid solution formation tendency based on the parameters of $\Delta S_{mix}/R$, ΔH_{mix}, δ, and Ω, without the parameter of $\delta(\Delta H_{mix})$. The empirical alloy parameters of AlCrTiV LW-MEA[15] also suggest high solid solution formation tendency. For the $Al_{38}Cr_{19}Fe_{19}Mn_{19}Ti_5$ LW-HEA,[13,14] the value of δ is higher than the threshold values for high solid solution formation tendency at $\delta \leqq 6.4$,[3] $\delta \leqq 6.5$,[38] and $\delta \leqq 6.6$,[21] however, a BCC phase formation is detected experimentally. For the Ti-containing alloys of

Table 2 Alloy parameters of $\Delta S_{mix}/R$, ΔH_{mix}, $\delta(\Delta H_{mix})$, δ and Ω for predicting the solid solution formation tendency in LW-HEA (Group E), Ti-containing alloys (Group G) and Al–Mg–Li and Al–Mg–Li–Ca alloys (Group F).

	Alloys	$\Delta S_{mix}/R$	ΔH_{mix}	$\delta(\Delta H_{mix})$	δ	Ω
	$Al_{20}Ti_{30}Li_{20}Mg_{10}Sc_{20}$	1.56	-0.4	28.3	5.3	42
	$Al_{38}Cr_{19}Fe_{19}Mn_{19}Ti_5$	1.46	-14.9	12.1	9.5	8.9
E	AlCrTiV	1.39	-16.8	15.0	6.4	8.8
	AlMgLiCaTi	1.61	4.8	28.0	12.1	6.0
G	AlMgLiTi	1.39	3.5	23.3	13.5	2.3
G	AlMgCaTi	1.39	0.3	29.4	13.0	3.3
	AlLiCaTi	1.39	5.5	35.8	13.5	2.3
	AlMgLi	1.10	-2.7	2.1	4.6	2.6
F	AlMgLiCa	1.39	-8.3	10.0	12.6	1.2
F	$Al_2MgLiCa$	1.33	-9.4	10.9	12.6	1.0
	$AlLiMgCa_{0.3}$	1.30	-5.2	5.7	9.4	1.7

AlMgLiCaTi, AlMgLiTi, AlMgCaTi, and AlLiCaTi alloys in Group G, the values of δ are higher than the threshold value for the solid solution formation. The value of $\delta(\Delta H_{mix})$ for the alloy in Group G is significantly large and positive, exceeding 20 kJ/mol. For the Al–Mg–Li and Al–Mg–Li–Ca alloys without Ti (Group F), the values of $\delta(\Delta H_{mix})$ are smaller than those of the alloys containing Ti (Group G), owing to the suppression of the deviation in the $\Delta H_{i\text{-}j}$ of the alloys in Group F. The δ values of the Al–Mg–Li–Ca alloys in Group F are almost equal to or slightly larger than that of the $Al_{38}Cr_{19}Fe_{19}Mn_{19}Ti_5$ LW-HEA in Group E. The ΔH_{mix} and $\delta(\Delta H_{mix})$ of the Al–Mg–Li–Ca alloys have low absolute values, suggesting high solid solution formation tendency. In the ΔH_{mix}-$\delta(\Delta H_{mix})$ map (Fig. 3), the equiatomic AlMgLi and quaternary Al–Mg–Li–Ca alloys exist in a region that overlaps with those of the 3d-HEAs (Group A) and RHEAs (Group B). Based on the above described discussion, the equiatomic AlMgLiCa and non-equiatomic composition $Al_2MgLiCa$ and $AlMgLiCa_{0.3}$ alloys imply high solid solution formation tendency in terms of the empirical alloy parameters related to the mixing enthalpy: ΔH_{mix}, $\delta(\Delta H_{mix})$, and Ω. The empirical alloy parameter related to the atomic radius (δ) suggests a negative tendency for solid solution formation in the Al–Mg–Li–Ca alloys. However, the δ values of the Al–Mg–Li–Ca alloys are similar to that of the $Al_{38}Cr_{19}Fe_{19}Mn_{19}Ti_5$ LW-HEA, for which solid solution formation occurs experimentally. It should be noted here that the $\delta(\Delta H_{mix})$ values of the Al–Mg–Li–Ca alloys are much smaller than those of the LW-HEAs and LW-MEAs (Group E) and the Ti-containing alloys (Group G).

3. Experimental Procedures

Table 3 shows the alloy compositions of the equiatomic AlMgLiCa and the non-equiatomic $Al_2MgLiCa$ and $AlMgLiCa_{0.3}$ alloys, which were tested to fabricate ingots by the casting process. Al (Mitsuwa Chemical Co., Ltd (Japan), grain size 5–8 mm, 99.99%), Mg (Kojyundo Chemical Laboratory Co., Ltd (Japan), wire-cuts $\phi 6 \times \sim 6$ mm, 99.9%), Li (Mitsuwa Chemical Co., Ltd (Japan), $\phi 10 \times 30$ mm, 99.9%), and Ca (Kojyundo Chemical Laboratory Co., Ltd. (Japan), grain size 1–3 mm, 99.5%) were used as the raw materials. A total amount of mixture of raw materials for the fabrication of the ingots was approximately 150 g. The mixture of raw materials was place in carbon crucibles with a flux for preventing oxidation during heating and melting. A thermal melt was obtained by the heating up to 1133 K under an inert gas. The ingots were obtained by metallic mold casting with a steel mold. The melting and casting processes included heating the mixture of the raw materials in a carbon crucible, melting the specimens in the carbon crucible, and pouring the thermal melt into a metallic mold. They were performed in an inert gas to prevent oxidation. The weight of the ingot was approximately 65 g, whereas the total weight of the mixture of raw materials was 150 g. The loss of the metallic elements during the melting and casting was due to the formation of slag and/or oxides via oxidation. The raw materials that remained in the crucible after casting were not detected visually in the present study. Figure 6 shows a schematic of the size of the metallic mold (Fig. 6(a)) and the positions of an ingot (Figs. 6(b1), 6(b2)). A step-shaped steel mold of 90-mm length and 40-mm width was used, where the depths at the thinnest part and thickest part were 22 mm and 28 mm, respectively (Fig. 6(a)). Melt-spun ribbons were prepared from a part of the ingots by the single-roller melt-spinning method using a silica nozzle. The fabrication was done at the Trans-Regional Corporation Center for Industrial Materials Research, Institute of Materials Research, Tohoku University, Japan.

Table 3 Alloy composition of equiatomic AlMgLiCa, non-equiatomic $Al_2MgLiCa$ and $AlMgLiCa_{0.3}$ alloys. (a) atomic percent, (b) weight percent.

(a) atomic percent, at. %

Alloys	Al	Mg	Li	Ca
AlLiMgCa	25.0	25.0	25.0	25.0
$Al_2LiMgCa$	40.0	20.0	20.0	20.0
$AlLiMgCa_{0.3}$	30.3	30.3	30.3	9.1

(b) weight percent, wt. %

Alloys	Al	Mg	Li	Ca
AlLiMgCa	27.4	24.7	7.1	40.8
$Al_2LiMgCa$	43.1	19.4	5.5	32.0
$AlLiMgCa_{0.3}$	38.4	34.6	9.9	17.1

The segregation during solidification cannot be ignored in multi-component alloys, including HEAs and MEAs, because the distribution coefficient of all constituent elements is hardly to be unity. In fact, the dendrite formation caused by the segregation in the ingots prepared by the casting process has been investigated experimentally and discussed using thermodynamic calculation for various HEAs and MEAs, including CoCrFeMnNi as a typical 3d-HEA,[45,46] RHEAs,[47] bio-HEAs,[48–50] and HE brasses.[51,52] The experimental technique of ingot splitting followed by microstructure analysis of a piece of an ingot is effective for the evaluation of the segregation and the inhomogeneous property in the constituent phases.[8,9] In this study, the ingots were cut into several parts, as shown in Fig. 6(b2), to investigate the

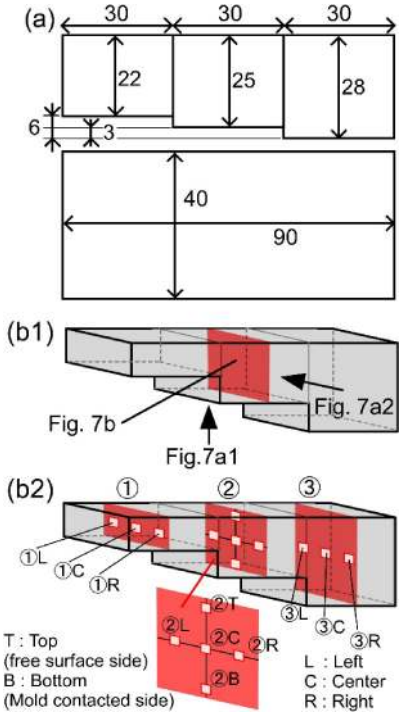

Fig. 6 The schematic illustration of the size of metallic mold (a), and the positions of the ingot (b1), (b2).

position dependences of the solidification microstructure. Each cut part was wet-polished using water-resistant emery paper. The hardness of each cut part was evaluated by the micro-Vickers hardness (*Hv*) test with a test force of 1 kgf. The measurement positions of the micro-Vickers test were randomly selected in each cut part, and seven points were measured. The hardness was evaluated by the average value and the standard deviation. Transmission electron microscopy (TEM) and scanning transmission electron microscopy (STEM) specimens of melt-spun ribbons were prepared by ion-milling technique.

4. Results and Discussion

Figure 7 shows the outer appearance (Figs. 7(a1), 7(a2)) and the cross-section image (Fig. 7(b)) of an ingot of the $Al_2MgLiCa$ alloy, where the ingots were prepared by the conventional crucible melting and mold-casting in air atmosphere. A part with metallic luster is observed at the mold contact surface, as shown in the outer appearance of the metallic mold contacted side (Fig. 7(a1)), for which the observation direction is depicted in Fig. 6(b1). A step-shaped ingot with a morphology corresponded to the step-shaped metallic mold is obtained by the casting process, as presented in the side view of the ingot (Fig. 7(a2)). Figure 7(b) shows the cross-section optical microscopy images of the ingots, without etching (the position was shown in Fig. 6(b1)). Oxidation is detected only on the surface region, and the inner part exhibits a typical metallic luster.

Table 4 shows the composition analysis results of various cut parts of an ingot of the $Al_2MgLiCa$ alloy obtained via inductively coupled plasma atomic emission spectroscopy (ICP-AES). The positions of the cut parts (①L·①C·①R, ②L·②C·②R, ③L·③C·③R) listed in the table are shown

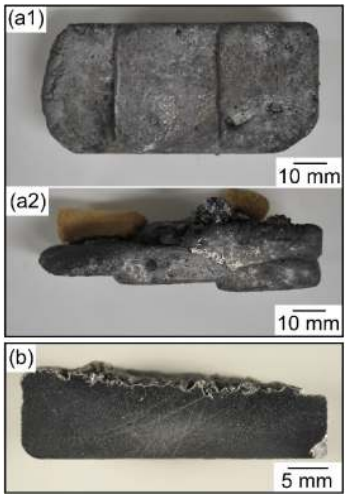

Fig. 7 The outer appearance (a1), (a2) and the cross-section image (b) of the ingot in $Al_2MgLiCa$ alloy.

Table 4 Composition analysis results in of various cut parts of the ingot in $Al_2MgLiCa$ alloy using ICP-AES. SD means standard deviation.

Position		Al	Mg	Li	Ca
①	L	48.68	23.87	12.74	14.71
	C	49.18	23.27	12.90	14.65
	R	48.90	23.48	13.14	14.48
②	L	48.70	23.65	13.15	14.50
	C	47.87	24.17	12.93	15.02
	R	46.82	24.72	13.11	15.35
③	L	49.02	23.19	13.29	14.50
	C	49.72	22.64	12.60	15.04
	R	49.37	22.82	13.24	14.58
Averege		48.70	23.53	13.01	14.76
SD		0.82	0.62	0.22	0.29

in Fig. 6(b2). A significant difference in the chemical composition analysis results of the cut parts is not observed. The average value of the chemical composition analysis results of the ingot yielded the composition of $Al_{48.70}Mg_{23.53}Li_{13.01}Ca_{14.76}$ (at%), whereas the nominal alloy composition is $Al_{40}Mg_{20}Li_{20}Ca_{20}$. According to the chemical composition analysis results, the Li and Ca contents in the ingots are slightly smaller than those in the nominal alloy composition. However, it is clarified that ingots with a large atomic ratio of Li and Ca without a macroscopic position dependence of the chemical composition were obtained by the conventional casting process. This involved conventional crucible melting without a vacuum chamber and pouring of the thermal melt into a steel mold.

Figure 8 shows the XRD patterns of various cut parts of an ingot of the $Al_2MgLiCa$ alloy. Figures 8(a) and 8(b) present these recorded at positions ①L, ①C, and ①R and ②L, ②C, and ②R, respectively. Figure 8(c) shows the XRD patterns at the seat positions of ③L, ③C, and ③R, and Fig. 8(d) shows that recorded at position ②C, together with the calculated intensities of the intermetallic compounds. Significant differences are not observed in the positions and number of sharp peaks in the XRD patterns obtained at positions ①L,

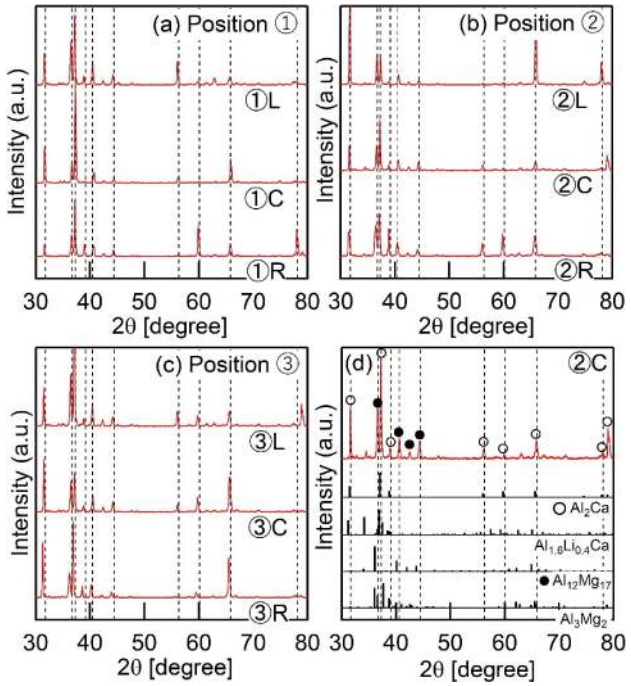

Fig. 8 XRD patterns of various cut parts of the ingot in $Al_2MgLiCa$ alloy. (a) positions of ①L, ①C and ①R, (b) positions of ②L, ②C and ②R, (c) positions of ③L, ③C and ③R, (d) position ②C, together with the calculated intensity of intermetallic compounds.

①C, and ①R (Fig. 8(a)); ②L, ②C, and ②R (Fig. 8(b)); and ③L, ③C, and ③R (Fig. 8(c)). In Fig. 8(d), most of the peaks can be identified as Al_2Ca (index ○) and/or $Al_{12}Mg_{17}$ (index ●). Some of the peaks are considered to correspond to $Al_{1.6}Li_{0.4}Ca$ or Al_3Mg_2. However, the existence of $Al_{1.6}Li_{0.4}Ca$ and Al_3Mg_2 cannot be concluded because of the overlap of the peak position with those of other intermetallic compounds and the weak peak intensity. These indicate the followings: (1) The main constituent phase in the ingots of the $Al_2MgLiCa$ alloy is not a single solid solution phase, but multiple intermetallic compounds. (2) There do not exhibit the macroscopic position dependence.

Figure 9 shows the SEM back-scattering electron (BSE) images to analyze the solidification microstructures of various cut parts of an ingot of the $Al_2MgLiCa$ alloy. The positions of ②C (Figs. 9(a), 9(b)), ②T, (Fig. 9(c)), and ②B (Fig. 9(d)) are depicted in Fig. 6(b2). Positions ②C, ②T, and ②B correspond to the central region of the ingot, free surface side, and metallic mold contacted side of the ingot, respectively. Figure 9(a2) shows the magnified image of Fig. 9(a1). In Fig. 9(b), the upper side corresponds to the free surface side. In Fig. 9(c), the lower side corresponds to the metallic-mold-contacted side. The solidification microstructure in the central region of the ingot (Fig. 9(a1)) indicated that a single phase structure was not obtained. The magnified image in Fig. 9(a2) displays that the white contrast phase with a facet is embedded in the gray contrast matrix. The randomly distributed black contrast regions correspond to the artifacts related with polishing and/or SiC polishing agent.[8,9] A multiphase structure composed of a white contrast facet phase and a gray contrast matrix is also observed at the free surface side (Fig. 9(b)) and metallic-mold-contacted side (Fig. 9(c)). The solidification structure becomes finer in the

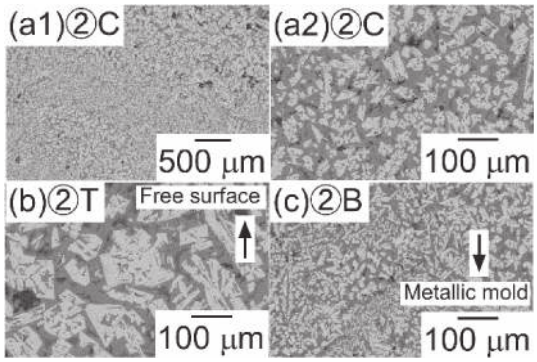

Fig. 9 Solidification microstructure of various cut parts of the ingot in $Al_2MgLiCa$ alloy. (a1), (a2) ②C, (b) ②T, (c) ②B. Figure 9(a2) was the magnified image of Fig. 9(a1).

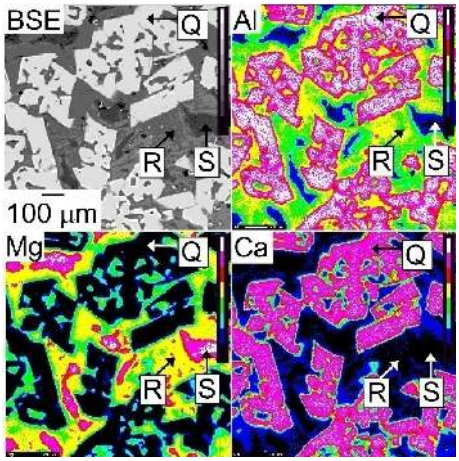

Fig. 10 Elemental mapping of the ingot in $Al_2MgLiCa$ alloy using EPMA-WDS. The position was corresponding to ②C in Fig. 6(b2).

order: mold contact area (Fig. 9(c)), central region of the ingot (Figs. 9(a1), 9(a2)), and free surface side (Fig. 9(b)), with the finest structure being in the mold contact area. The size of the solidification structure is dependent on the cooling rate during the solidification, so that a fine solidification microstructure is observed in the metallic-mold-contacted region. These trends indicate that the solidification structure of the ingots of the $Al_2MgLiCa$ alloy is a multi-phase structure, regardless the position in the ingots. Furthermore, the size of the solidification structure presented cooling rate dependence.

Figure 10 shows the elemental mapping of the ingot of the $Al_2MgLiCa$ alloy obtained via EPMA–WDS, in which the position corresponds to ②C. Al and Ca are enriched in the white-contrast facet phase in the SEM–BSE image (index Q), whereas the Mg content is poor. The elemental mapping in Fig. 10 suggests that the gray-contrast matrix in the SEM–BSE image, which is displayed in Fig. 9, is constructed with regions R and S with different chemical compositions. Both regions R and Q contain Al and Mg; however, the concentration of Ca is poor. The Al and Mg concentration in regions R and Q exhibit differences. Table 5 summarizes the chemical composition analysis results using WDS in the Al/Mg/Ca atomic composition ratio at regions Q, R, and S. The Al/Ca ration in region Q is approximately 2/1. The Al/Mg ratio in region R is over 1, whereas that in region S is

Table 5 Al/Mg/Ca atomic composition ratio of the regions Q, R, S in Fig. 10.

Region		Al	Mg	Ca
Q	Dendrite	63.3	4.1	32.6
R	Inter-dendrite	51.2	44.3	4.6
S	Inter-dendrite	35.9	63.3	0.8

below 1. The solidification microstructure analysis results obtained via XRD, SEM, and chemical composition analysis by EPMA indicate that the solidification microstructure in the ingots of the $Al_2MgLiCa$ alloy is constructed with the Al_2Ca (Q) and the composites of Al–Mg intermetallic compound matrix (R and S), where the ingots were prepared by the conventional crucible melting and mold-casting in air atmosphere.

Figure 11 shows the Vickers hardness (*Hv*) values of various cut parts of an ingot of the $Al_2MgLiCa$ alloy. A significant difference in the *Hv* values at ①L, ①C, ①R; ②L, ②C; ②; and ③L, ③C, and ③R is not observed. Position dependence of the average value of *Hv* is not detected, whereas the standard deviation of *Hv* is large. The standard deviation of *Hv* is explained by the difference in the hardness of the constituent phases of the ingots. The measured *Hv* value varies because the solidification structure is coarse compared to the size of the Vickers indentation and the volume fraction of constituent phases in the indentation region was different in each position. Here, it should be noted that the negligible position dependence of the average value of *Hv* in the ingots corresponds to the small position dependence of the chemical composition, constituent phases, and solidification microstructure.

The experimental technique involving ingot splitting and microstructure analysis of a piece of an ingot,[8,9] including the OM observation in the cross section of the ingots (Fig. 7), chemical composition analysis by ICP-AES (Table 4), XRD (Fig. 8), solidification microstructure analysis by SEM-BSE images (Fig. 9), and element mapping (Fig. 10) with chemical composition analysis (Table 5) by EPMA-WDS, is effective for evaluating the macroscopic position dependences of the chemical compositions and the solidification microstructures of the ingots in Al–Mg–Li–Ca alloys, where the ingots were prepared by the conventional crucible melting and mold-casting in air atmosphere. The corresponding results are summarized as follows: (1) The macroscopic position dependence of the chemical compositions of the ingots was small. (2) Although the chemical compositions of Ca and Li slightly decreased in comparison with the nominal composition, ingots containing Al, Mg, Li, and Ca were obtained by the casting process. (3) The position dependences of the constituent phases of the ingots were not detected. (4) Instead of a single solid solution phase, multi-intermetallic compounds were formed in the ingots. (5) The solidification microstructure was not dependent on the position in the ingots. (6) The solidification microstructure became finer with the increase in the cooling rate during the solidification. The position dependences of the chemical composition, constituent phases, and solidification microstructure were negligible, resulting in a small deviation in the average value of *Hv* in the ingots (Fig. 11).

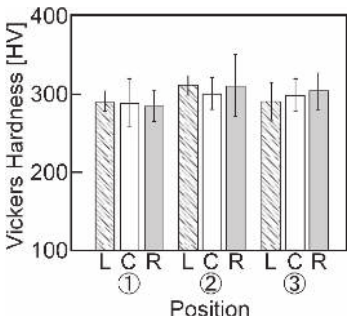

Fig. 11 Vickers Hardness (Hv) of various cut parts of the ingot in $Al_2MgLiCa$ alloy.

Macroscopic position dependences of the constituent phases and the chemical compositions were not observed in the ingots of the $AlCoCrFeNi_{2.1}$ eutectic HEAs (EHEAs) via the experimental technique of ingot splitting followed by microstructure analysis of a piece of an ingot.[8,9] This characteristic was similar to that of the ingots of the $Al_2MgLiCa$ alloy in the present study. For the $AlCoCrFeNi_{2.1}$ EHEAs, the solidification microstructure in the melt-spun ribbons prepared by the single-roller melt-spinning method with a cooling rate of $\sim 10^5$ K/s[53] was found to be significantly different from that in the metallic mold casting ingots formed with a cooling rate of 80–600 K/s. It also varied from that in the furnace cooling formed ingots with a cooling rate of ~1 K/s.[8,9] In contrast, the constituent phases in $AlCoCrFeNi_{2.1}$ EHEAs was not dependent on the cooling rate. Rapid solidification may cause changes in the solidification microstructure and the constituent phases of the Al–Mg–Li–Ca alloys. In the present study, the solidification microstructures of the melt-spun ribbons of the $Al_2MgLiCa$ alloys were investigated by focusing on the difference between the rapidly solidified specimens and the metallic mold casting ingots. Figure 12 shows the XRD patterns of a metallic mold casting ingot with the position ②C (as-cast) and of rapidly solidified melt-spun ribbons (melt-spun ribbons)[54] of the $Al_2MgLiCa$ alloy. The sharp peaks in the

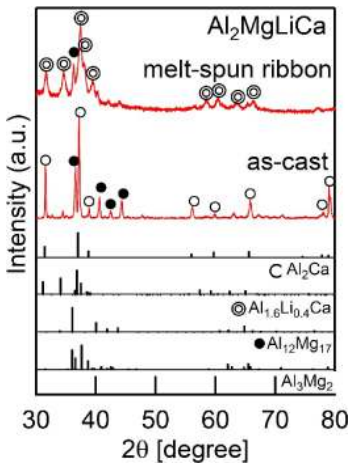

Fig. 12 XRD patterns of the ingot (as-cast) and rapidly solidified melt-spun ribbons (melt-spun ribbon) in $Al_2MgLiCa$ alloys. XRD pattern of the ingot was obtained from the central region of the ingot, and that of melt-spun ribbons was obtained from the finely-powdered specimens.

XRD pattern of the melt-spun ribbons cannot be assigned to a single solid solution phase. The main constituent phase in the melt-spun ribbons is identified as $Al_{1.6}Li_{0.4}Ca$ (index ◎) and $Al_{12}Mg_{17}$.[55] The rapid solidification leads to a change in the Laves phase from Al_2Ca (metallic mold casting ingots) to $Al_{1.6}Li_{0.4}Ca$ (melt-spun ribbons) in the $Al_2MgLiCa$ alloy. The Laves phase formation cannot be suppressed by the rapid solidification, resulting that a single solid solution was not obtained and the composite of $Al_{1.6}Li_{0.4}Ca$ and Al–Mg-rich intermetallic compounds was formed in the melt-spun ribbons of the $Al_2MgLiCa$ alloy.

Figure 13 shows the TEM-bright field (BF) image (Fig. 13(a)) and selected area diffraction (SAD) pattern (Fig. 13(b)) of the melt-spun ribbons of the $Al_2MgLiCa$ alloy.[54] TEM-BF image exhibits the formation of a nano-crystalline structure in the melt-spun ribbons. The SAD pattern shows the Debye rings corresponding to this nano-crystalline structure. Figure 14 presents the STEM-high-angle annular dark field (HAADF) image (Fig. 14(a)) and EDS element mapping (Fig. 14(b)) of the melt-spun ribbons of the $Al_2MgLiCa$ alloy. Region S presents a tendency to be enriched in Mg while being poor in Al and Ca. In contrast, Al and Ca are enriched in region T. The XRD analysis (Fig. 12) and the TEM (Fig. 13) and STEM (Fig. 14) analyses clarify the characteristics of the solidification microstructures of melt-spun ribbons of the $Al_2MgLiCa$ alloy: (1) a single solid solution is not obtained. (2) the constituent phase is slightly changed by rapid solidification, however, a composite of an Al–Ca-based Laves phase and Al–Mg intermetallic compounds is formed in the melt-spun ribbons as well as the ingots. (3) A nano-crystalline structure is formed in the melt-spun ribbons.

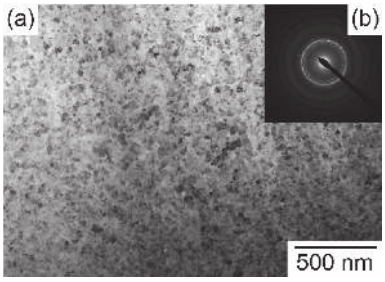

Fig. 13 TEM microstructure of the melt-spun ribbons in $Al_2MgLiCa$ alloy. (a) BF image, (b) SAD pattern.

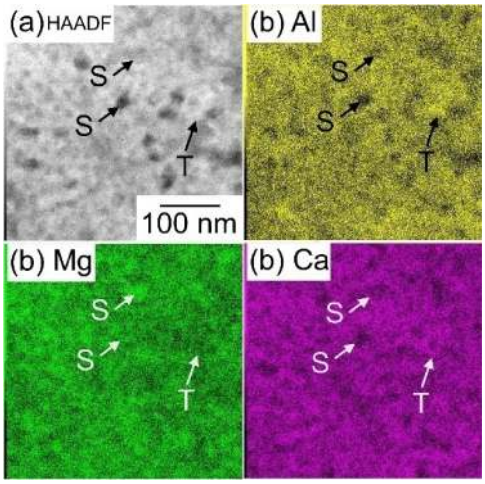

Fig. 14 STEM-HAADF image (a) and elemental mapping obtained by STEM-EDS (b) of the melt-spun ribbons in $Al_2MgLiCa$ alloy.

The $Al_2MgLiCa$ alloy was designed to decrease ΔH_{mix} and $\delta(\Delta H_{mix})$ simultaneously. In terms of the empirical alloy parameters of ΔH_{mix}, $\delta(\Delta H_{mix})$, and δ, the solid solution formation tendency in the $AlMgLiCa_{0.3}$ alloy is higher than those of the equiatomic AlMgLiCa and $Al_2MgLiCa$ alloys, as can be seen from Table 2 and Fig. 5. To investigate the composition dependence on the solid solution formation tendencies of Al–Mg–Li–Ca alloys, the XRD patterns of the ingots of the $AlMgLiCa_{0.3}$ and $Al_2MgLiCa$ alloys were investigated. Figure 15 shows XRD patterns of the ingots of the equiatomic AlMgLiCa, non-equiatomic $Al_2MgLiCa$, and $AlMgLiCa_{0.3}$ alloys. The XRD patters of the AlMgLiCa and $AlMgLiCa_{0.3}$ alloys were obtained from the central regions of the ingots, whereas that of the $Al_2MgLiCa$ alloy was acquired from position ②C. The XRD pattern of the equiatomic AlMgLiCa alloy are similar to those in the XRD pattern of the $Al_2MgLiCa$ alloy, and the main constituent phases of the former are identified as Al_2Ca and $Al_{12}Mg_{17}$. The peak positions in the XRD pattern of the $AlMgLiCa_{0.3}$ alloy are different from those in the XRD patterns of the equiatomic AlMgLiCa and $Al_2MgLiCa$ alloys. A composite of Al_2Ca, $Al_{12}Mg_{17}$, Al_3Mg_2, and $Al_{1.6}Li_{0.4}Ca$ is formed in the ingot of the $AlMgLiCa_{0.3}$ alloy. These results highlight the difficulty in the fabrication of the ingots of the Al–Mg–Li–Ca alloys with a single solid solution by the casting process with the conventional crucible melting and mold-casting in air atmosphere. Formation of the Al_2Ca and $Al_{1.6}Li_{0.4}Ca$ Laves phases is observed in the ingots (Fig. 8, Fig. 15). In the Al–Ca binary phase diagram,[56] Al_2Ca is a Laves phase with a congruent melting temperature. The melting temperature of Al_2Ca (1079 degree Celsius, °C) is higher than those of Al (660°C) and Ca (842°C). $Al_{1.6}Li_{0.4}Ca$ is also a Laves phase.[55] In general, a Laves phase is known to be formed in alloys when there is a significant difference in the atomic radii of the constituent elements.[57] Focusing on the δ values

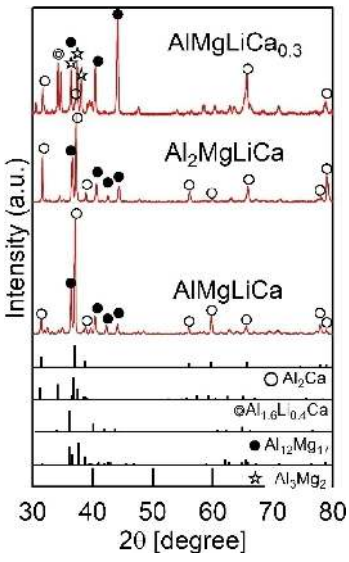

Fig. 15 XRD patterns of the ingot in equiatomic AlMgLiCa, non-equiatomic $Al_2MgLiCa$ and $AlMgLiCa_{0.3}$ alloys. The XRD patters were obtained from the center of the ingots.

of the Al–Mg–Li–Ca alloys (The difference in the atomic radii of the constituent elements in multi-component alloys can be evaluated by the δ parameter), those of the equiatomic AlMgLiCa, non-equiatomic $Al_2MgLiCa$, and $AlMgLiCa_{0.3}$ alloys were larger than the threshold value of δ for solid solution formation. The Laves phase formation in the ingots and the melt-spun ribbons of the Al–Mg–Li–Ca alloys was considered to be related to the large deviation in the atomic radii of the constituent elements, while Al–Mg–Li–Ca alloys was considered to show the high solid solution formation tendency from the view point of the ΔH_{mix} and $\delta(\Delta H_{mix})$ parameters.

In this paper, the followings were discussed for the development of LW-HEAs and LW-MEAs as casting materials: (1) the alloy design of LW-HEAs and LW-MEAs as casting materials, and (2) the fabrication of the ingots of the Al–Mi–Li–Ca LW-MEAs to clarify where the application of casting process in LW-HEAs and LW-MEAs is available or not. The alloy parameter, $\delta(\Delta H_{mix})$, was suggested for evaluating the deviation in the $\Delta H_{i\text{-}j}$ values of the constituent elements and the difficulty in the melting and casting processes of the multi-component alloys. Thus far, significant differences have not been reported in the ΔH_{mix} values of the typical HEAs (3d-HEAs and RHEAs) and LW-HEAs and LW-MEAs. The $\delta(\Delta H_{mix})$ values of previously developed LW-HEAs and LW-MEAs are similar to those of the liquid-phase-separation-type amorphous alloys (Table 1, Table 2, Fig. 3), indicating the difficulty in their fabrication via melting and the casting process. New Al–Mg–Li–Ca alloys were designed for decreasing the $\delta(\Delta H_{mix})$ parameter whose values were similar to that in 3d-HEAs and RHEAs (Table 1, Table 2, Fig. 3). By considering the $\delta(\Delta H_{mix})$ parameter for evaluating the difficulty in the application of casting process, new Al–Mg–Li–Ca alloys without large positive $\Delta H_{i\text{-}j}$ values of their constituent elements can be designed. The ingots of the equiatomic AlMgLiCa, and non-equiatomic $Al_2MgLiCa$ and $AlMgLiCa_{0.3}$ alloys could be obtained by the casting process with the conventional crucible melting and mold-casting in air atmosphere, by the decrease in the difficulty in the casting process. From the view point of single solid solution formation, single solid solution formation did not occur and laves phase formation was detected in Al–Mg–Li–Ca alloys. This was considered to be related to the large difference in the atomic radius among constituent elements of the Al–Mg–Li–Ca alloys. The present study demonstrates that the difficulty in the application of casting process in LW-HEAs and LW-MEAs can be decreased by using the $\delta(\Delta H_{mix})$ parameter, and the ingots of LW-HEAs and LW-MEAs can be obtained by the conventional crucible melting and mold-casting in air atmosphere without both distinct equipment and a vacuum chamber.

5. Conclusions

The hardest obstacle in the development of LW-HEAs and LW-MEAs is the difficulty in the fabrication process. The fabrication of the ingots of LW-HEAs and LW-MEAs by the casting process was investigated because the casting process has the advantage of the ability of mixing elements of multi-component alloys at the atomic level. In particular, the following two topics were examined: (1) alloy design of LW-HEAs and LW-MEAs, (2) the fabrication of the ingots of the Al–Mi–Li–Ca LW-MEAs to clarify where the application of casting process in LW-HEAs and LW-MEAs is available or not. The present study demonstrated that ingots of LW-MEAs could be obtained by the conventional casting process via crucible melting without both expensive equipment and a vacuum chamber and by mold casting under air atmosphere. The obtained results are summarized as follows:

(1) The alloy parameter of $\delta(\Delta H_{mix})$ was suggested for evaluating the deviation in the $\Delta H_{i\text{-}j}$ values of the constituent elements of the considered multi-component alloys.

(2) The parameter, $\delta(\Delta H_{mix})$, was effective for discussing the solid solution tendencies of the multi-component alloys. The value of $\delta(\Delta H_{mix})$ in LW-MEAs and LW-HEAs reported to date were significantly different from that in 3d-HEAs and RHEAs. In the ΔH_{mix}-$\delta(\Delta H_{mix})$ map, the LW-HEAs and the LW-MEAs occupied a region similar to that of the liquid-phase-separation-type amorphous alloys. In contrast, in the ΔH_{mix}-$\delta(\Delta H_{mix})$ map, the positions of the Al–Mg–Li–Ca alloys, which were designed in the present study, overlapped the positions of the 3d-HEAs and RHEAs. Al–Mg–Li–Ca alloys were considered to be the alloys with higher solid solution formation tendency from the viewpoint of ΔH_{mix} and $\delta(\Delta H_{mix})$ than previously reported LW-HEAs and the LW-MEAs.

(3) The parameter, $\delta(\Delta H_{mix})$, was also effective for evaluating the difficulty in the casting process of the multi-component alloys. The alloys with small absolute values of ΔH_{mix} and large positive values of $\delta(\Delta H_{mix})$ experienced difficulty in the fabrication of the ingots by casting, because of the increase in the vapor pressures of the constituent elements due to the large positive $\Delta H_{i\text{-}j}$. The decrease in the $\delta(\Delta H_{mix})$ of the multi-component LW-MEAs resulted in the realization of the fabrication of their ingots by the conventional casting process without both expensive equipment and a vacuum chamber.

(4) In an ingot of the $Al_2MgLiCa$ LW-MEA prepared by the conventional crucible melting and mold-casting in air atmosphere, the chemical composition analysis clarified that Li and Ca were slightly reduced compared to the nominal composition. Significant position dependences of the chemical composition, solidification microstructure, and constituent phases in the ingots were not detected. No significant position dependency was observed for the average value of the Vickers hardness.

(5) Ingots with a single solid solution phase were not obtained for the equiatomic AlMgLiCa, non-equiatomic $Al_2MgLiCa$, and $AlMgLiCa_{0.3}$ alloys, where the ingots were obtained by the conventional crucible melting and mold-casting in air atmosphere. Rapidly solidified specimens of the $Al_2MgLiCa$ alloy could be obtained by the single roller melt-spinning method. A single solid solution phase was not obtained in the melt-spun ribbons of the $Al_2MgLiCa$ alloy. The main constituent phases of the ingots of the $Al_2MgLiCa$

alloy were Al_2Ca and Al–Mg-rich compounds, whereas $Al_{1.6}Li_{0.4}Ca$ and Al–Mg-rich compounds were formed in its melt-spun ribbons. The large positive δ value of the $Al_2MgLiCa$ alloy was considered to correspond to the formation of a Laves phase. Besides ΔH_{mix} and $\delta(\Delta H_{mix})$, the δ parameter was also important for the alloy design of the LW-HEAs and the LW-MEAs.

Acknowledgements

A part of this research was carried out with the support of the research grant from the Japan Foundry Engineering Society (JFS), and JSPS KAKENHI (grant number 18K04750, 19H05172). The authors are grateful to Dr. K. Amiya at Trans-Regional Corporation Center for Industrial Materials Research, Institute of Materials Research, Tohoku University for the help with the fabrication of melt-spun ribbon, and to Prof. S. Kobayashi at Graduate School of Science and Engineering, Ehime University for the help with Vickers Hardness measurements.

REFERENCES

1) B. Cantor, I.T.H. Chang, P.K. Night and A.J. Vincent: Mater. Sci. Eng. A **375** (2004) 213–218.
2) J.W. Yeh, S.K. Chen, S.J. Lin, J.Y. Gan, T.S. Chin, T.T. Shun, C.H. Tsau and S.Y. Chang: Adv. Eng. Mater. **6** (2004) 299–303.
3) Y. Zhang, Y.J. Zhou, J.P. Lin, G.L. Chen and P.K. Liew: Adv. Eng. Mater. **10** (2008) 534–538.
4) S. Ranganathan: Curr. Sci. **85** (2003) 1404–1406. https://www.currentscience.ac.in/Downloads/article_id_085_10_1404_1406_0.pdf.
5) B.S. Murty, J.-W. Yeh and S. Ranganathan: *High-Entropy Alloys*, 1st Edition, (Elsevier, Amsterdam, 2014).
6) M.C. Gao, J.-W. Yeh, P.K. Liaw and Y. Zhang: *High-Entropy Alloys: Fundamentals and Applications*, 1st Edition, (Springer, Berlin, 2016).
7) D.B. Miracle and O.N. Senkov: Acta Mater. **122** (2017) 448–511.
8) T. Nagase, M. Takemura, M. Matsumuro and T. Maruyama: J. JFS **89** (2017) 119–129.
9) T. Nagase, M. Takemura, M. Matsumuro and T. Maruyama: Mater. Trans. **59** (2018) 255–264.
10) T. Nagase: J. Soc. Mech. Eng. **121** (2018) 8–11.
11) T. Nagase, T. Kakeshita, K. Matsumura, K. Nakazawa, S. Furuya, N. Ozoe and K. Yoshino: Mater. Des. **184** (2019) 108172.
12) K.M. Youssef, A.J. Zaddach, C. Niu, D.L. Irving and C.C. Koch: Mater. Res. Lett. **3** (2015) 95–99.
13) R. Feng, M.C. Gao, C. Lee, M. Mathes, T. Zuo, S. Chen, J.A. Hawk, Y. Zhang and P.K. Liaw: Entropy **18** (2016) 333.
14) R. Feng, M.C. Gao, C. Zhang, W. Guo, J.D. Poplawsky, F. Zhang, J.A. Hawk, J.C. Neuefeind, Y. Ren and P.K. Liaw: Acta Mater. **146** (2018) 280–293.
15) Y. Qiu, Y.J. Hu, A. Taylor, M.J. Styles, R.K.W. Marceau, A.V. Ceguerra, M.A. Gibson, Z.K. Liu, H.L. Fraser and N. Birbilis: Acta Mater. **123** (2017) 115–124.
16) R. Li, J. Gao and K. Fan: Mater. Sci. Forum **650** (2010) 265–271.
17) X. Du, R. Wang, C. Chen, B. Wu and J.C. Huang: Key Eng. Mater. **727** (2016) 132–135.
18) T. Nagase, A. Shibata, M. Matsumuro and M. Takemura: Reports of JILM Meeting **135** (2018) 55.
19) O. Maulik, D. Kumar, S. Kumar, S. Kumar Dewangan and V. Kumar: Mater. Res. Express **5** (2018) 052001.
20) M. Niinomi: J. JFS **73** (2001) 784–790.
21) M. Niinomi and M. Nakai: J. JILM **67** (2017) 307–313.
22) T. Sato: J. JFS **73** (2001) 791–797.
23) Y. Tamaki and T. Miyazaki: Nihon Hotetsu Shika Gakkai Zasshi **42** (1998) 528–539.
24) M. Niinomi, H. Fukui, T. Takeuchi and S. Katsura: J. JFS **73** (2001) 798–804.
25) A. Takeuchi and A. Inoue: Mater. Trans. **46** (2005) 2817–2829.
26) S. Guo, Q. Hu, C. Ng and C.T. Liu: Intermetallics **41** (2013) 96–103.
27) X. Yang and Y. Zhang: Mater. Chem. Phys. **132** (2012) 233–238.
28) O.N. Senkov, G.B. Wilks, D.B. Miracle, C.P. Chuang and P.K. Liaw: Intermetallics **18** (2010) 1758–1765.
29) O.N. Senkov, J.M. Scotta, S.V. Senkova, D.B. Miracle and C.F. Woodward: J. Alloy. Compd. **509** (2011) 6043–6048.
30) O.N. Senkov, J.M. Scott, S.V. Senkova, F. Meisenkothen, D.B. Miracle and C.F. Woodward: J. Mater. Sci. **47** (2012) 4062–4074.
31) A. Inoue: Acta Mater. **48** (2000) 279–306.
32) Y. Nakagawa: Acta Metall. **6** (1958) 704–711.
33) A.A. Kundig, M. Ohnuma, D.H. Ping, T. Ohkubo and K. Hono: Acta Mater. **52** (2004) 2441–2448.
34) B.J. Park, H.J. Chang, D.H. Kim and W.T. Kim: Appl. Phys. Lett. **85** (2004) 6353–6355.
35) N. Mattern, U. Kuhn, A. Gebert, T. Gemming, M. Zinkevich, H. Wendrock and L. Schultz: Scr. Mater. **53** (2005) 271–274.
36) T. Nagase, M. Suzuki and T. Tanaka: J. Alloy. Compd. **619** (2015) 267–274.
37) T. Nagase, M. Suzuki and T. Tanaka: Intermetallics **61** (2015) 56–65.
38) T. Nagase, M. Suzuki and T. Tanaka: J. Alloy. Compd. **619** (2015) 332–337.
39) T. Nagase, M. Suzuki and T. Tanaka: J. Alloy. Compd. **619** (2015) 311–318.
40) T. Nagase, T. Terai, T. Kakeshita, M. Matsumoto and Y. Fujii: Mater. Trans. **60** (2019) 554–560.
41) T. Nagase, T. Terai, T. Kakeshita and K. Morita: Mater. Trans. **61** (2020) 311–317.
42) T. Nagase and Y. Umakoshi: J. Alloy. Compd. **650** (2015) 342–350.
43) T. Nagase and Y. Umakoshi: J. Alloy. Compd. **649** (2015) 1174–1181.
44) T. Nagase, M. Takemura, M. Matsumuro, M. Matsumoto and Y. Fujii: Mater. Des. **117** (2017) 338–345.
45) M. Laurent-Brocq, A. Akhatova, L. Perriere, S. Chebini, X. Sauvage, E. Leroy and Y. Champion: Acta Mater. **88** (2015) 355–365.
46) K. Takashima, T. Maruyama and T. Nagase: Reports of JFS Meeting **170** (2017) 37.
47) M.C. Gao, C.S. Carney, O.N. Dogan, P.D. Jablonksi, J.A. Hawk and D.E. Alman: JOM **67** (2015) 2653–2669.
48) T. Nagase, M. Todai, T. Hori and T. Nakano: J. Alloy. Compd. **753** (2018) 412–421.
49) T. Nagase, K. Mizuuchi and T. Nakano: Entropy **21** (2019) 483.
50) T. Nagase, K. Mizuuchi, M. Todai and T. Nakano: Materia Japan **58** (2019) 78.
51) K.J. Laws, C. Crosby, A. Sridhar, P. Conway, L.S. Koloadin, M. Zhao, S. Aron-Dine and L.C. Bassman: J. Alloy. Compd. **650** (2015) 949–961.
52) T. Nagase, A. Shibata, M. Matsumuro, M. Takemura and S. Semboshi: Mater. Des. **181** (2019) 107900.
53) T. Nagase, M. Takemura and M. Matsumuro: Mater. Sci. Forum **879** (2017) 1350–1354. http://www.ttp.net/978-3-0357-1129-5/23.html.
54) T. Nagase, A. Terayama, T. Nagaoka, N. Fuyama and K. Amiya: Microscopy **67**(S2) (2018) i35.
55) R. Nesper and G.J. Miller: J. Alloy. Compd. **197** (1993) 109–121.
56) *Binary Alloy Phase Diagrams*, II Ed., ed. by T.B. Massalski, "Al–Ca", 1, (ASM International, Materials Park, 1990) p. 130.
57) E. Fujita: *Kinzoku Butsuri*, (Agne Gijutsu Center, Tokyo, 1996).